Experimental and theoretical study of phase separation in ZnPc:C$_{60}$ blends

Tobias Mönch [a],[*], Tejas S. Sherkar [c], L. Jan Anton Koster [c], Pascal Friederich [d],
Moritz Riede [a],[1], Peter Formanek [b], Christian Koerner [a], Koen Vandewal [a],
Wolfgang Wenzel [d], Karl Leo [a]

[a] Institut für Angewandte Photophysik, TU Dresden, George-Bahr-Str. 1, 01069 Dresden, Germany
[b] Leibniz-Institut für Polymerforschung Dresden e. V., Hohe Str. 6, 01069 Dresden, Germany
[c] Zernike Institute for Advanced Materials, University of Groningen, Nijenborgh 4, 9747 AG Groningen, The Netherlands
[d] Institut für Nanotechnologie, Karlsruher Institut für Technologie, Hermann-von-Helmholtz-Platz 1, Eggenstein-Leopoldshafen, 76344 Germany

ARTICLE INFO

ABSTRACT

Understanding the relationship between the absorber layer microstructure and the power conversion efficiency is of paramount importance to further improve the efficiency of organic solar cells. Utilizing transmission electron microscopy (TEM), (photo)conductive atomic force microscopy ((p)cAFM), 3D drift diffusion simulations, and density functional theory, we reveal the microscopic origins of phase separation in a blend of zinc phthalocyanine (ZnPc) and C$_{60}$, used as an absorber layer in organic solar cells. By means of (p)cAFM, we observe photoconductive, circular structures at the surface, which are identified as α ZnPc islands. Moreover, in agreement with TEM investigations, we observe photoconductive, nanorod like structures close to the surface which we assign to β ZnPc. Finally, we apply a 3D drift diffusion simulation based on the morphology determined by TEM to provide a link between the different contrasts observed in pcAFM and TEM.

1. Introduction

Organic solar cells have the potential to contribute to the world's future demand for energy with the specific advantage of large area and low cost roll to roll processing. Through the development of new materials and new device concepts such as multi junction cells, organic solar cells have reached power conversion efficiencies of up to 12% [1].

A grand challenge of organic solar cells is to split strongly bound photo excitations, called excitons, which are created by the absorbed sunlight. The binding energy of such bound electron hole pairs is generally much larger than the thermal energy at room temperature. Hence, to split the excitons into free charge carriers, an energy step is introduced via a donor acceptor heter ojunction made of two different materials [2].

In addition, to overcome the low exciton diffusion length [3], the donor and acceptor materials are mixed e.g. by thermal co evaporation in vacuum to form a nanoscale bulk heterojunction (BHJ) [4,5]. By depositing the BHJ layer on a heated substrate, kept at a specific substrate temperature (T_{sub}), the phase separation of the two components can be controlled.

The as such created morphology should at least fulfill two opposing requirements in a balanced manner: First, the neat ma terial phases should be small, with dimensions comparable to the exciton diffusion length to guarantee that most of the excitons

reach the heterointerface. Second, the neat material phases should be large enough to provide closed pathways for the free charge carriers to the respective electrodes, making large domains favorable. In the worst case, such an interpenetrating network may also exhibit isolated islands, which do not have a connection to an electrode and, thus, facilitate recombination of the charge carriers. Hence, for an optimized exciton harvesting, it is important to understand the relationship between processing conditions, thin film growth, and device parameters.

In this work, we study the thin film growth of donor:acceptor blends composed of the donor molecule zinc phthalocyanine (ZnPc, $C_{32}H_{16}N_8Zn$) [6] and the acceptor molecule C_{60} [7] via transmission electron microscopy (TEM) and photoconductive atomic force microscopy (pcAFM), at a mixing ratio of ZnPc:C_{60} 2:1 (by volume, thickness 40 nm) deposited at a substrate temperature of T_{sub} 150 °C. We choose these specific processing parameters to maximize the domain sizes of the material phases, facilitating their observation. Moreover, we use density functional theory (DFT) [8,9] to develop a first principles model for the interaction of ZnPc with C_{60}. We then perform numerical 3D drift diffusion simulations to rationalize the experimental findings. Using this combined experimental and theoretical approach, we are able to distinguish the two different phases of ZnPc (metastable α phase and β phase) within the blend and correlate their structural attributes to electro optical properties.

We find that the surface of the thin film is α phase ZnPc rich [10], while β phase ZnPc [11] is mainly present in the bulk of the blend. This analysis is difficult to achieve by X ray diffraction as the Bragg reflections are often not resolvable [12]. Furthermore, DFT calculations suggest that the formation of ZnPc stacks (β phase) is promoted by the presence of C_{60} due an induced dipole moment in the fullerene and a hence increased binding energy between the ZnPc molecules. Briefly, we observe a minimization of the $Zn-N$ distance of two adjacent molecules as expected in the β phase of ZnPc. In addition, we perform 3D drift diffusion modeling of the ZnPc:C_{60} absorber layer based on the morphology observed in TEM and an organic solar cell prepared at similar conditions. The excellent agreement between experimental data and simulation allows us to explain the locally increased (photo)conductivity determined by the pcAFM measurements.

2. Materials and methods

All samples are prepared in a custom made multi chamber ultra high vacuum system (BESTEC, Berlin, Germany) with a base pressure of $p < 10^{-8}$ mbar. The indium tin oxide coated glass (ITO; Thin Film Devices, Anaheim, USA; 90 nm thickness; sheet resistance 30 $\Omega/\square$) is cleaned with NMP (N Methyl 2 pyrrolidone), ethanol, and a plasma cleaner step and is subsequently used as a substrate for the ZnPc:C_{60} blends in the pcAFM measurements. In addition, a SiO$_2$ coated Cu Mesh (400 mesh, purchased from Ted Pella, Inc., USA) serve as substrates for the TEM specimens. The TEM samples are either kept in vacuum or inert nitrogen atmosphere prior to the measurement.

ZnPc (purchased from ABCR, Karlsruhe, Germany; thin film density: 1.55 g cm^{-3}) and C_{60} (from CreaPhys, Dresden, Germany; thin film density: 1.63 g cm^{-3}) are purified by vacuum gradient sublimation prior to device fabrication and then thermally co evaporated in one preparation step on the respective substrates to minimize the experimental uncertainties. The thickness of the blend layer is 40 nm, determined by two independent quartz crystal monitors, one for each material. During the co evaporation of the ZnPc and C_{60}, the substrate temperature (T_{sub}) is kept at T_{sub} 150 °C. The geometry of the set up is described in Ref. [22].

To minimize the influence of ambient air on the electro optical

properties [13], AFM [14] measurements are carried out in a nitrogen flushed gascell (AIST NT, Apeldoorn, Netherlands). The measurements are done with a PtSi coated tip (PtSi CONT; k 0.2 N·m^{-1}, work function W_F 4.72 5.18 eV [15]; from Nano and More; Wetzlar, Germany). The sample was illuminated by a violet laser (STARF50, Roithner Lasertechnik, Vienna, Austria, P 50 mW, λ 450 nm, attenuated with an OD 2 filter) and focused by a 20× objective (Nikon CFI SPLFL WD 20XC, Nikon Instruments Europe B.V., Germany). Further experimental details about pcAFM can be found in Refs. [16–18]. The AFM images are analyzed using the free, open source software gwyddion [19].

The TEM investigations were performed in a Libra200 (Carl Zeiss Microscopy GmbH, Oberkochen, Germany) equipped with an in column imaging filter at an acceleration voltage of 200 kV.

First, the diffraction patterns were recorded at low dose conditions (500 e·nm^{-2}). Subsequently, the morphology and chemical composition were investigated at high dose illumination (5,00,000 e·nm^{-2}). In all specimens the crystalline structure quickly decays even at low dose illumination, but the morphology remains stable at high dose so that elemental mapping was possible. To increase the contrast, some images were recorded at a defocus of approximately 2 μm.

3. Results and discussion

The phase transition of ZnPc from the α ZnPc modification (island like growth) [20] to the β ZnPc modification (nanorod like growth) [21] is known to occur either at elevated substrate temperatures during the deposition or via post annealing steps [22–24]. The main difference between the α and the β ZnPc modification is the distance between the central Zn atom and N atoms of two adjacent molecules, which is minimal in β phase ZnPc [25]. The structural transition from α to β ZnPc leads to different optical [21], electrical [26], and microstructural [27] properties.

On one hand, growing crystalline β ZnPc nanorods with their long axis perpendicular to the substrate surface [28,24], with C_{60} in between the nanorods would be desirable for efficient charge carrier transport to the electrodes in organic solar cells [29], if the surface roughness remains lower than the thickness of adjacent layers. On the other hand, this geometric arrangement would massively reduce the molecular contact between ZnPc and C_{60}, as shown by DFT calculations for different adsorption configurations of CuPc (which has comparable structure to ZnPc [12]) and C_{60} by Ren et al. [27].

3.1. Transmission electron microscopy

Placing the TEM grid with the copper bars facing the material crucibles at the bottom of the vacuum chamber, results in the patterning of the SiO$_2$ substrate (shadow masking) as shown in Fig. 1. The TEM micrograph displays three different areas denoting the three simultaneously deposited layers at T_{sub} 150 °C: the red region is a pristine layer of ZnPc, the green region is a pristine layer of C_{60}, and the yellow region is the 2:1 blend of the ZnPc and C_{60}. All thin films are deposited at the same time, in one single evaporation step, and the same substrate temperature. Additional images showing separately prepared pristine and blend layers, including TEM elemental maps can be found in the supplementary information Appendix A.1 and Appendix A.2.

The pristine layer of ZnPc (red region) shows almost no discernible structure, indicating a nearly amorphous ZnPc layer. On the other side, the pristine C_{60} tends to agglomerate in islands [30], as previously reported by our group [18].

From Fig. 1 we derive typical feature parameters such as the equivalent disc radius (defined as the radius of a disc with the same
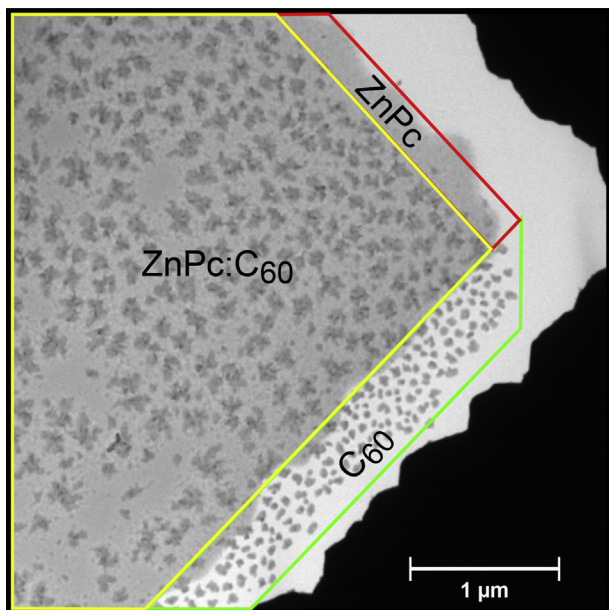
Fig. 1. TEM bright field micrograph where 40 nm ZnPc:C_{60} (2:1, T_{sub} 150 °C, yellow marked region) are deposited. The pure ZnPc (red marked region) and C_{60} (green marked regions) regions originate from mesh shadow effects. (For interpretation of the references to colour in this figure legend, the reader is referred to the web version of this article.)

Fig. 2. TEM bright field micrograph showing ZnPc:C_{60} blend layer. The diffraction pattern of the two different areas are depicted in Figs. 3 and 4.

projected area as the grain) and the nearest neighbor distance (NND, defined as the distance between the centers of the equiva lent disc radius discs), see Table 1. Although these values are significantly larger than typical exciton diffusion length in disor dered materials (3 100 nm [31]), those structures might provide closed transport paths for the separated charge carriers and exhibit lower disorder compared to the amorphous background.

Zooming into the blend layer (Fig. 2; yellow marked region in Fig. 1) shows an island like growth of aggregates embedded in an apparently structureless background, with small nanorods sticking out of agglomerates. The size of those nanorods (width 17 34 nm, length 71 128 nm) is in good agreement with the measurements of Chowdhury et al. [24] of a pristine ZnPc layer deposited on glass and subsequently annealed at 300 °C. Therefore, we attribute these nanorods to pristine β phase ZnPc and the structureless background to a homogeneous mixture of ZnPc and C_{60}. The diffraction patterns of an agglomerate (area 1) and the structureless background (area 2) are shown in Fig. 3 and Fig. 4. These two diffraction pattern clearly show the spatial in homogeneity and locally dependent crystallinity of the blend layer, which should result in locally different opto electronical proper ties. The indexed diffraction pattern of Figs. 3 and 4 match the re flections of ZnPc and C_{60} determined by X ray diffraction as shown in Table 2.

The partial occurrence of elliptically shaped β phase ZnPc in the presence of C_{60} was already observed previously by Kim et al. [34], who carried out GISAXS and GIWAXS experiments on ZnPc:C_{60} blends deposited at room temperature. Comparing to Kim et al. [34], we deploy a higher substrate temperature and a higher ZnPc
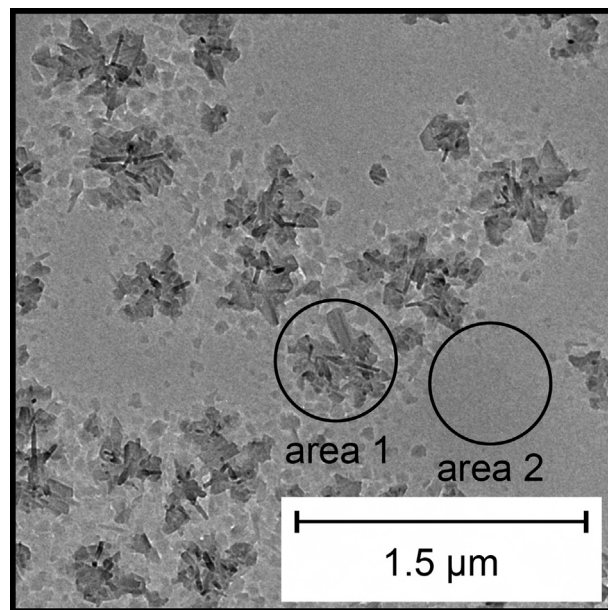
volume fraction, increasing the diffusion length of the ZnPc mole cules, yielding larger ZnPc crystallites. Hence, our observation is in good agreement with Kim et al. Moreover, we suppose that C_{60} plays in important role for the phase separation in ZnPc:C_{60} blends [35].

Furthermore, we attribute the featureless background (area 2 in Fig. 2) to a homogeneous mixture of ZnPc:C_{60}, which may contain locally ZnPc or C_{60} rich domains as observed by Simon et al. [36] and Schindler et al. [37], deposited at T_{sub} RT. In conclusion, we observed the growth of β ZnPc nanorods in the presence C_{60} rich domains. Moreover, we observed spatial variations in the crystal linity of the blend layer.

3.2. Density functional theory calculations

To probe the hypothesis that C_{60} plays a major role in the pro cess of phase separation in the ZnPc:C_{60} blend at this substrate temperature, we carried out DFT calculations for different molec ular configurations. We used the RIDFT approach [38] implemented in TURBOMOLE [39] on a B3 LYP [40]/SV(P) [41] level of theory including Grimme corrections [42].

In these calculations, we compare the binding energy of two ZnPc molecules to the binding energy of two ZnPc molecules on top of a C_{60} fullerene. The ZnPc:ZnPc pair potentials are shown in Fig. 5. The relative position of the two ZnPc molecules was obtained by geometry optimization of the dimer with and without the fullerene. Note that the total energy is set to zero for large ZnPc:ZnPc distances.

In presence of a fullerene molecule, the binding energy of the ZnPc dimer is 86 meV larger than the binding energy of an isolated ZnPc dimer. At a substrate temperature of T_{sub} 150 °C, this will

Table 1
Characteristic statistical parameters of different regions highlighted in Fig. 1.

Statistical quantity	Pristine C_{60} region	Pristine ZnPc region	ZnPc:C_{60} blend region
Eq. disc radius	39.7 ± 14.1 nm	n.a.	99.2 ± 29.8 nm
NND	148.8 ± 36.3 nm	n.a.	276.8 ± 70.4 nm
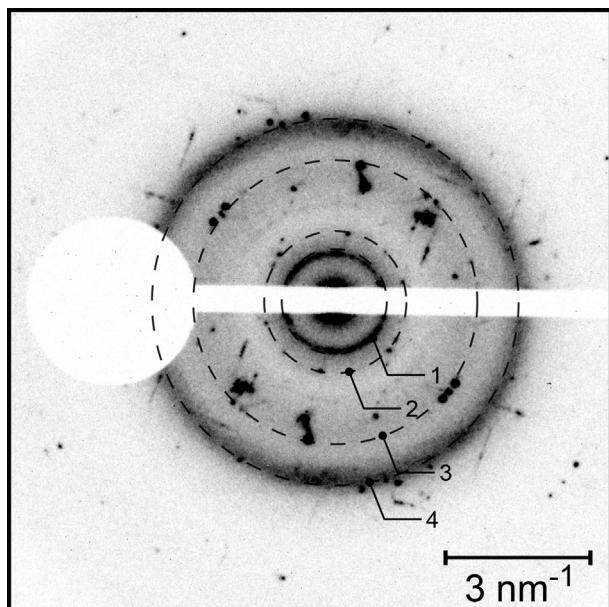
Fig. 3. TEM diffraction pattern of area 1 shown in Fig. 2.

lead to the preferential aggregation of ZnPc on C_{60} and result in the growth of more stable ZnPc stacks on C_{60} than in isolation. The microscopic mechanism of this process is the induction of a dipole moment in the highly polarizable, delocalized π cloud of the fullerene molecule. In our calculations we observe an induced dipole moment of 2.7 D at an equilibrium distance of 6 Å between the center of mass of the fullerene and the ZnPc molecule. This dipole moment leads to an attractive force between the positively charged Zn atom and the electron density on the fullerene facing towards the ZnPc molecule. The induced dipole moment attracts and binds the second ZnPc molecule, which provides a mechanism for the experimentally observed phase separation in the ZnPc:C_{60} blend.
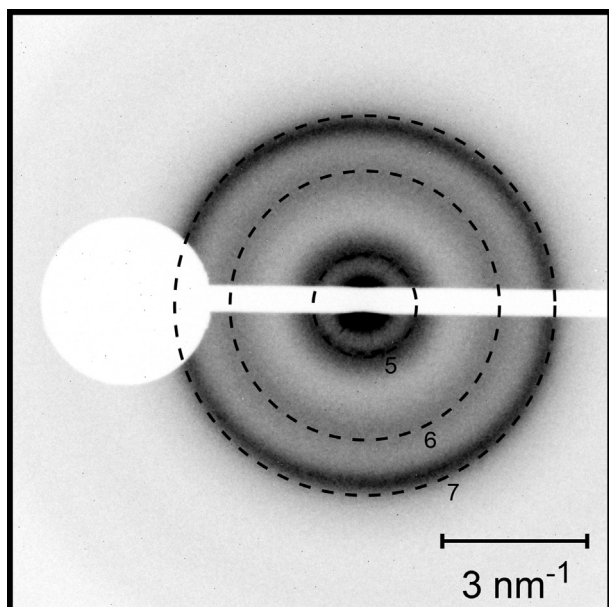
No.	Lattice plane distance (hkl)	Material
1	12.3 Å(200)	ZnPc [32]
2	8.4 Å(111)	C_{60} [33]
3	4.3 Å(311)	C_{60} [33]
4	3.4 Å	ZnPc or C_{60}
5	12.2 Å(200)	ZnPc [32]
6	4.7 Å(311)	C_{60} [33]
7	3.3 Å	ZnPc or C_{60}

3.3. (Photo)conductive atomic force microscopy

We use pcAFM to verify the findings of the TEM measurements and relate them to electro optical properties. With this technique, local (photo)currents and topography are mapped simultaneously with high spatial resolution (~ 25 nm).

Fig. 6 shows a pcAFM image of the topography and the respec tive short circuit current distribution at the surface of the blend layer. First of all, the weak correlation between the surface topog raphy and short circuit map indicates the complex morphology of the blend layer, where different material domains resemble each other in similar surface topography. Moreover, as there are neither topographical nor electrical indications of the nanorod like struc tures as compared to Fig. 1, we conclude that they are buried in the bulk of the blend layer.

Nevertheless, the surface topography and the short circuit cur rent map show round structures, which can be attributed to α ZnPc rich domains as shown for pristine ZnPc layers by Kozlik et al. [21]. Moreover, we substantiate the attribution to α ZnPc rich do mains, as the ZnPc PtSi [43,15] contact exhibits a lower barrier compared to the C_{60} PtSi contact. Hence, pcAFM experimentally map the ZnPc rich domains in contact with the AFM tip. Without pcAFM, it would be difficult to distinguish α ZnPc and C_{60}, as both materials tend to grow in spherical shapes resulting in a similar topography and diffraction pattern [21,44,30,12]. We attribute the structures with lower photoconductivity to domains with disad vantageous (e.g. standing) ZnPc molecule orientation relative to C_{60} molecules, lowering the absorption and the exciton dissociation efficiency [27]. On larger length scales, the short circuit current is

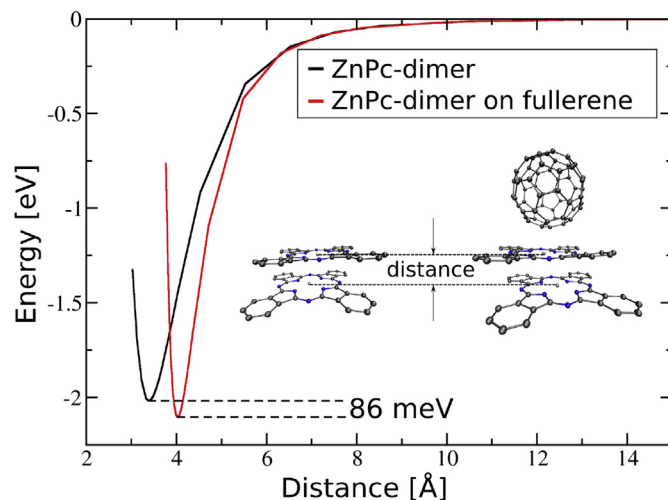**Fig. 4.** TEM diffraction pattern of area 2 shown in Fig. 2.

Fig. 5. Binding energy of ZnPc-dimer with and without a C_{60} fullerene. The equilib rium distance of the two adjacent ZnPc molecules is larger in presence of a fullerene but 86 meV lower in energy and therefore considerably more stable at room tem perature. This leads to aggregation of ZnPc stacks and nucleation of the beta-phase of ZnPc in the vicinity of C_{60} fullerenes.
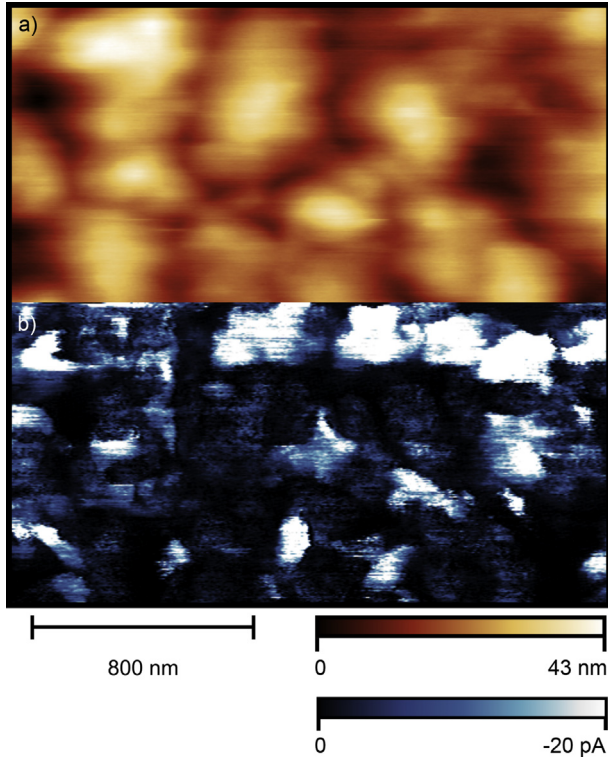
Fig. 6. Simultaneously recorded AFM topography (a) and short-circuit current distribution (b) at the ZnPc:C$_{60}$ surface. Areas with increased short-circuit current can be attributed to ZnPc-rich domains.

Fig. 7. Simultaneously measured AFM topography (a) and short-circuit current distribution (b) after increasing the tip-sample interaction. The red marked structures highlight ZnPc-rich nanorods. (For interpretation of the references to colour in this figure legend, the reader is referred to the web version of this article.)
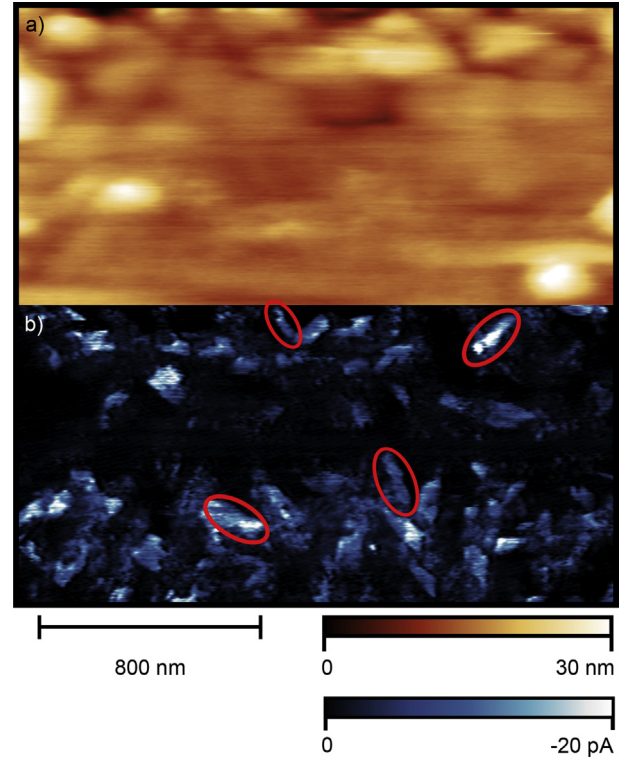
altered by the stoichiometry between ZnPc and C$_{60}$, locally varying crystallinity *etc.* Nevertheless, domains with high photoconductivity are ZnPc rich, whereas no photoconductivity indicates domains with a C$_{60}$ layer in contact with the AFM tip. Thus the locally varying crystallinity observed in TEM (Figs. 3 and 4) has a minor influence on the short circuit current maps.

To explore the sub surface for the β ZnPc nanorods observed in TEM, we take advantage of the usually undesired strong interaction between the AFM tip and the sample in contact mode. By significantly increasing the tip sample force, we indent into the sample while scanning over the surface.

Fig. 7 a shows the modified surface of the ZnPc:C$_{60}$ blend after scanning the surface. Now, the surface topography is smoother as compared to Fig. 6 a, but no nanorods are visible in the topographic image. Two possible explanations for this phenomenon are: *i)* the AFM tip is blunt and the nanorods are below the resolution limit of the tip or *ii)* The nanorods are embedded in the surface and do not give topographic information.

In contrast, Fig. 7 b reveals similarly shaped nanorods as observed in TEM. Thus, we attribute those structures to β ZnPc nanorods, as their similar shape and dimensions (length 100 160 nm, diameter 35 40 nm) correlate with the previously observed nanorods in TEM. Obviously, these structures are hidden beneath the original surface of the sample.

Compared to the metastable α ZnPc at the surface, the photoconductivity of the β ZnPc nanorods is slightly lower. The area averaged short circuit current at the surface (Fig. 6) is 5 pA and 3 pA in the bulk (Fig. 7), as the areal fraction of β ZnPc is significantly lower than the α ZnPc fraction. In contrast, the studies of Roy et al. suggest a higher (photo)conductivity of the β ZnPc compared to α ZnPc. This deviation may originate from the material adsorption at the AFM tips apex, increasing the tip sample

resistance. In contrast to this, the dark current map Fig. 8 b reveals increased current distribution over the β ZnPc nanorods, which is expected from the aforementioned energy level considerations (cf. table A.3) and the observation of locally increased crystallinity (Figs. 3 and 4).

To summarize, we observed the nanoscopic short circuit and dark current over ZnPc rich domains in ZnPc:C$_{60}$ blends. By measuring with low tip sample interaction, we observe α ZnPc domains at the surface of the blend, and by further indenting the sample, β ZnPc domains in the bulk of the sample. Thus, consistently with the bulk TEM measurements, we attribute the nanorod shaped structures to β ZnPc domains. Moreover, the observed β ZnPc nanorods in ZnPc:C$_{60}$ blends appear at significantly lower temperatures compared to the structural transition in pristine ZnPc layers [26,21,45].

3.4. 3D drift diffusion simulations

To link the features observed in TEM (Fig. 2) and pcAFM (Fig. 7) and relate them to a macroscopic solar cell measurement (Fig. A.17), we perform 3D drift diffusion simulations based on the morphology shown in Fig. 2.

To model the electron and hole currents (J_e and J_p) in the absorber layer, we use the J V curve of a solar cell stack which can be found in Appendix A.4. Note that the substrate temperature during deposition of the organic solar cell is slightly lower than for the TEM and pcAFM measurements. Therefore, the density of the pure material phases in this organic solar cell might be lower than in the TEM and pcAFM samples. The model solves the exciton diffusion equation within the donor (ZnPc) phase. For simplicity, the exciton generation rate is assumed to be uniform throughout
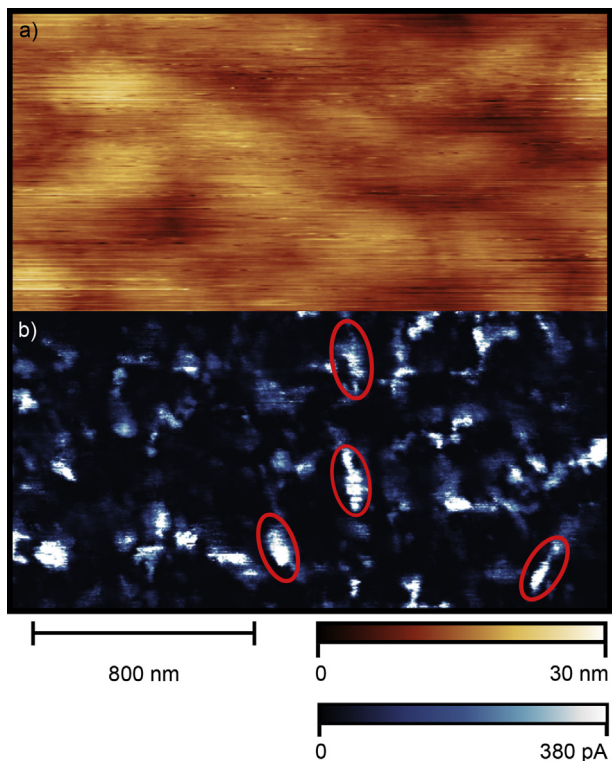
Fig. 8. Simultaneously measured AFM topography (a) and dark-current at U 1 V (b) at a different position on the sample after increasing the tip-sample interaction. The red marked structures highlight ZnPc-rich nanorods. (For interpretation of the references to colour in this figure legend, the reader is referred to the web version of this article.)

Fig. 9. Simulated hole current density map (J_p) at the cathode under short-circuit condition for a ZnPc:C$_{60}$ (2:1) blend. In agreement with the pcAFM measurements (Fig. 7), the highest short-circuit current is observed at the β-ZnPc nanorods.

the absorber layer, a good approximation as discussed in Ref. [46]. The method for 3D modeling of the morphology starting from a 2D image and the electro optical input parameters can be found in Appendix A.3. Each grid point in the 3D morphology is either assigned as pure donor or as an intricate mixture of donor and acceptor (*i.e.* mixed phase).
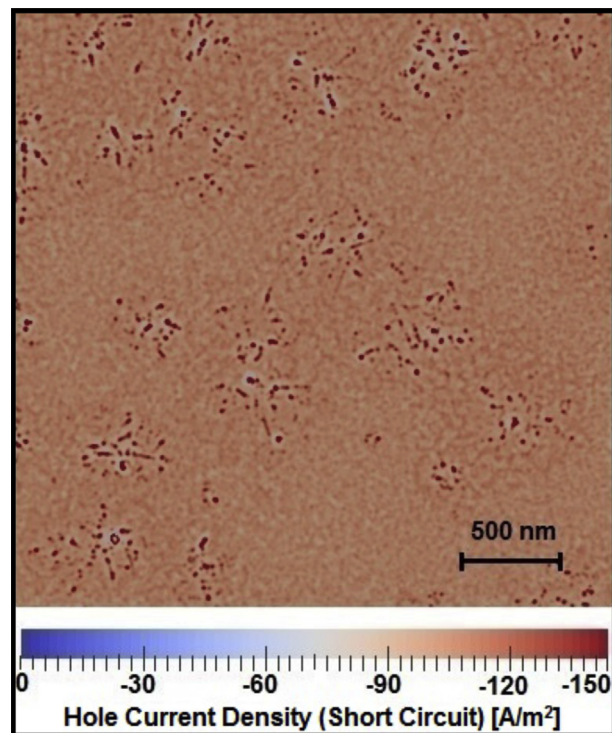
The high degree of mixing of donor and acceptor in the blend layer guarantees the absence of pure acceptor. If the acceptor concentration at a grid point is below 16%, it is indexed as pure donor. Above this threshold, it is considered as mixed phase. The quenching efficiency of the excitons in the mixed phase and at the electrodes is 100%. The generation rate of both carriers on either side of the ZnPc:C$_{60}$ interface is equal and depends only on the exciton diffusion constant and the local exciton density. Moreover, free charges are created at the ZnPc:C$_{60}$ interface with the gener ation rate as stated in Ref. [47]. The ZnPc phase consists of only holes whereas the mixed phase contains holes and electrons. The free charge carriers can also recombine in a bimolecular way with the recombination rate constant given by the modified Langevin expression [47].

$$\gamma \quad \gamma_{\mathrm{pre}} \frac{q}{\varepsilon} (\mu_e + \mu_h), \qquad (1)$$

where q is the elementary charge, ε is the dielectric constant, and the Langevin prefactor γ_{pre} is a fit parameter.

The transport of the free charge carriers away from the interface is governed by drift and diffusion. The electrostatic potential is solved from the Poisson equation. For further details, see Ref. [47].
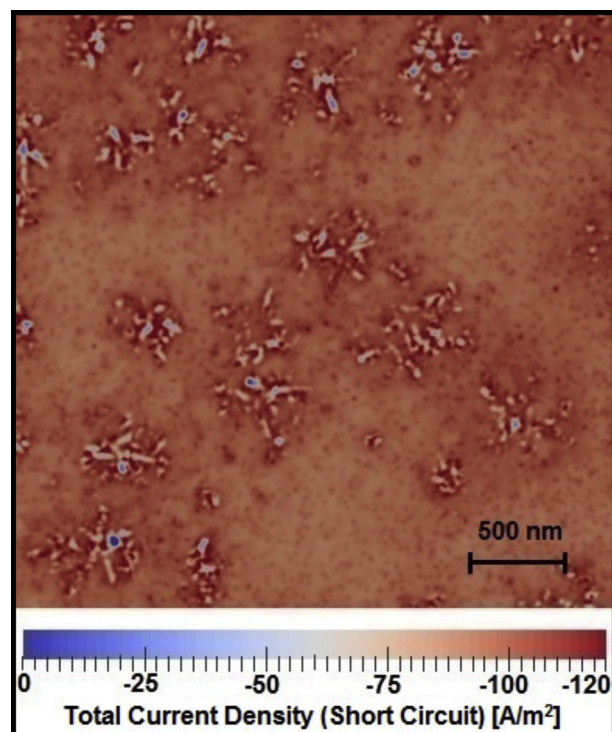
The evolution of electron and hole mobilities as a function of the donor concentration [48] is shown in Fig. A.14. For all intermediate donor concentrations, the mobility is calculated by interpolation of the logarithm of the mobility (μ).

The total simulation volume is 26 million points

Fig. 10. Simulated, current density map ($J_p + J_e$) at the cathode under short-circuit condition for a simulated ZnPc:C$_{60}$ (2:1) blend.
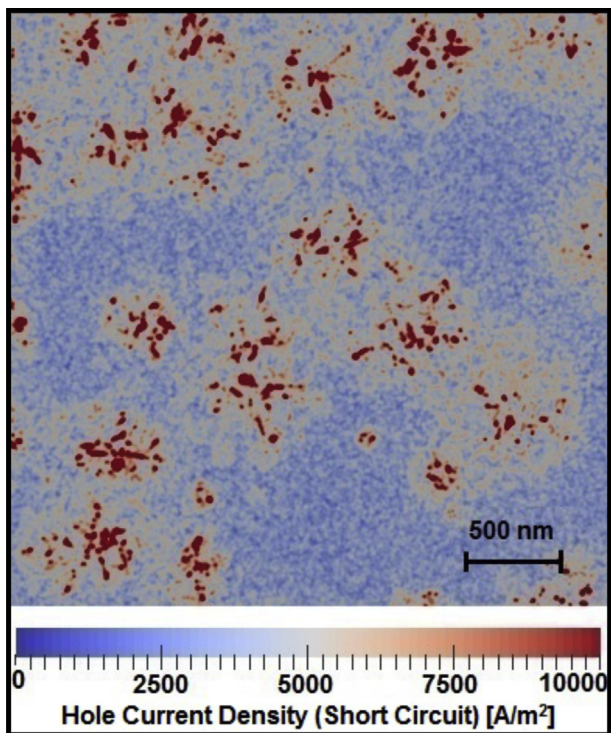
Fig. 11. Simulated, dark-current density map (J_p) at the cathode with an applied forward bias 1 V, for a simulated ZnPc:C_{60} (2:1) blend.

($26 \times 1000 \times 1000$) with a grid spacing of $\Delta x = \Delta y = \Delta z = 3.2$ nm. The simulated J-V curve based on the discretized TEM image and the experimentally determined J-V of the organic solar cells are shown in Appendix A.4.

The Langevin prefactor ($\gamma_{pre} = 0.03$) is the only fit parameter extracted after fitting the simulation result to the experimental J-V curve. The reduced bimolecular recombination rate relative to the Langevin expression can be attributed to the phase separation of ZnPc and the formation of crystalline structures.

Our simulations are able to explain the locally increased (photo)conductivity found in the pcAFM measurements in terms of the locally dependent material mixing ratio as shown in Fig. 9 in combination with the AFM tip. There, the hole only current at short circuit current conditions is imaged. In agreement with the pcAFM measurements, we observe the largest hole current at the β ZnPc nanorods. Thus, we prove the chemical selectivity of pcAFM to ZnPc rich domains. The electron and hole currents under short circuit current condition are shown in Fig. 10, illustrating a major contribution of the mixed phase to the overall short circuit current. Nevertheless, these currents can not be resolved as they are below the resolution of the AFM tip.

Fig. 11 shows the simulation of the current density under dark conditions at 1 V applied bias in forward direction. In agreement with Fig. 8 the current density is maximal across the β ZnPc nanorods. The reason is the high work function of the AFM tip used, which results in blocking of electrons and leads to hole current flowing through the β ZnPc nanorods.

4. Conclusions

We experimentally investigated the phase separation in ZnPc:C_{60} blend deposited at $T_{sub} = 150$ °C by means of TEM and pcAFM. Moreover, we utilized computational simulations to rationalize the findings from the experiments and give microscopic explanations.

With both pcAFM and TEM, we observed nanorod shaped structures which we attribute to β phase ZnPc. More specifically, as TEM predominantly probes the bulk of the sample, we increased the tip-sample force in the pcAFM measurement to indent into the sample surface, where very (photo)conductive β ZnPc nanorods are observed. On the surface, we observed photoconductive, circular/spherical like shaped structures, which we attribute to α ZnPc. Overall, both ZnPc phases exhibit a comparable photoconductivity.

To link the different contrast mechanisms observed in TEM and pcAFM, we discretized a TEM image in terms of locally varying ZnPc:C_{60} mixing ratios to obtain a simple 3D model of the blend layer, which is subsequently used in a 3D drift-diffusion simulation. This simulation confirms the findings of the pcAFM measurements that the photoconductive regions are ZnPc rich. Hence, *i)* pcAFM maps the hole current of the ZnPc:C_{60} blend, *ii)* discriminates between ZnPc and C_{60}, and *iii)* the enhanced phase separation yields reduced recombination rate relatively to the Langevin expression.

To understand the phase separation, we performed DFT calculations of the ZnPc:C_{60} blend. We observe that C_{60} favors the growth of stable ZnPc stacks which can be explained by the attractive force between the central Zn atom and the C_{60} molecules and the induced dipole moment of the C_{60} molecules. Hence, our study provides detailed insights into the relationship between phase separation in ZnPc:C_{60} blends and the processing parameters (T_{sub} and mixing ratio). Finally, the observed flat lying down, very photoconductive, highly crystalline β ZnPc nanorods may also potentially be interesting for the application in high performance organic field effect transistors.

Appendix A. Supplementary data

Supplementary data related to this article can be found at http://dx.doi.org/10.1016/j.orgel.2015.09.023.

References

[1] Heliatek, Heliatek consolidates its technology leadership by establishing a new world record for organic solar technology with a cell efficiency of 12% Http://www.heliatek.com/newscenter/latest_news/neuer-weltrekord-fur-organische-solarzellen-heliatek-behauptet-sich-mit-12-zelleffizienz-als-technologiefuhrer/?lang=en#.

[2] C.W. Tang, Two-layer organic photovoltaic cell, Appl. Phys. Lett. 48 (2) (1986) 183, http://dx.doi.org/10.1063/1.96937. http://link.aip.org/link/APPLAB/v48/i2/p183/s1&Agg=doi.

[3] B.P. Rand, J. Xue, S. Uchida, S.R. Forrest, Mixed donor-acceptor molecular heterojunctions for photovoltaic applications. I. Material properties, J. Appl. Phys. 98 (12) (2005) 124902, http://dx.doi.org/10.1063/1.2142072. http://link.aip.org/link/JAPIAU/v98/i12/p124902/s1&Agg=doi.

[4] M. Hiramoto, H. Fujiwara, M. Yokoyama, Three-layered organic solar cell with

a photoactive interlayer of codeposited pigments, Appl. Phys. Lett. 58 (10) (1991) 1062, http://dx.doi.org/10.1063/1.104423. http://scitation.aip.org/content/aip/journal/apl/58/10/10.1063/1.104423.

[5] G. Yu, J. Gao, J.C. Hummelen, F. Wudl, A.J. Heeger, Polymer photovoltaic cells: enhanced efficiencies via a network of internal donor-acceptor heterojunctions, Science 270 (5243) (1995) 1789 1791, http://dx.doi.org/10.1126/science.270.5243.1789. http://adsabs.harvard.edu/abs/1995Sci...270.1789Y.

[6] D.D. Eley, Phthalocyanines as semiconductors, Nature 162 (4125) (1948) 819, http://dx.doi.org/10.1038/162819a0. http://www.nature.com/doifinder/10.1038/162819a0.

[7] H.W. Kroto, J.R. Heath, S.C. O'Brien, R.F. Curl, R.E. Smalley, C60: Buckminsterfullerene, Nature 318 (6042) (1985) 162 163, http://dx.doi.org/10.1038/318162a0. http://www.nature.com/nature/journal/v318/n6042/ris/318162a0.ris.

[8] I. Beljakov, V. Meded, F. Symalla, K. Fink, S. Shallcross, M. Ruben, W. Wenzel, Spin-crossover and massive anisotropy switching of 5d transition metal atoms on graphene nanoflakes, Nano Lett. 14 (6) (2014) 3364 3368, http://dx.doi.org/10.1021/nl500872c. http://pubs.acs.org/doi/abs/10.1021/nl500872c.

[9] M. Lukas, V. Meded, A. Vijayaraghavan, L. Song, P.M. Ajayan, K. Fink, W. Wenzel, R. Krupke, Catalytic subsurface etching of nanoscale channels in graphite, Nat. Commun. 4 (2013) 1379, http://dx.doi.org/10.1038/ncomms2399. http://www.nature.com/doifinder/10.1038/ncomms2399.

[10] F. Iwatsu, Size effects on the. alpha.-. beta. transformation of phthalocyanine crystals, J. Phys. Chem. 92 (6) (1988) 1678 1681. http://pubs.acs.org/doi/abs/10.1021/j100317a057.

[11] W.R. Scheidt, W. Dow, Molecular stereochemistry of phthalocyanatozinc (II), J. Am. Chem. Soc. 99 (4) (1977) 1101 1104, http://dx.doi.org/10.1021/ja00446a021. http://pubs.acs.org/doi/pdf/10.1021/ja00446a021.

[12] C. Schünemann, C. Elschner, A. Levin, M. Levichkova, K. Leo, M. Riede, Zinc phthalocyanine influence of substrate temperature, film thickness, and kind of substrate on the morphology, Thin Solid Films 519 (11) (2011) 3939 3945, http://dx.doi.org/10.1016/j.tsf.2011.01.356. http://linkinghub.elsevier.com/retrieve/pii/S0040609011004214.

[13] J. Šebera, P. Fitl, J. Vlcek, M. Vrňata, F. Fendrych, J. Kopecek, I. Kratochvílová, Interaction of selected gases with zinc phthalocyanine thin films: theoretical and experimental studies, Eur. Phys. J. Appl. Phys. 64 (1) (2013) 10202, http://dx.doi.org/10.1051/epjap/2013120188. http://www.epjap.org/10.1051/epjap/2013120188.

[14] G. Binnig, C.F. Quate, C. Gerber, Atomic force microscope, Phys. Rev. Lett. 56 (9) (1986) 930 933, http://dx.doi.org/10.1103/PhysRevLett.56.930. http://link.aps.org/doi/10.1103/PhysRevLett.56.930.

[15] M. Niranjan, S. Zollner, L. Kleinman, A. Demkov, Theoretical investigation of PtSi surface energies and work functions, Phys. Rev. B 73(19). doi:10.1103/PhysRevB.73.195332. URL http://link.aps.org/doi/10.1103/PhysRevB.73.195332

[16] D.C. Coffey, O.G. Reid, D.B. Rodovsky, G.P. Bartholomew, D.S. Ginger, Mapping local photocurrents in polymer/fullerene solar cells with photoconductive atomic force microscopy, Nano Lett. 7 (3) (2007) 738 744, http://dx.doi.org/10.1021/nl062989e. http://pubs.acs.org/doi/abs/10.1021/nl062989e.

[17] B.H. Hamadani, N. Gergel-Hackett, P.M. Haney, N.B. Zhitenev, Imaging of nanoscale charge transport in bulk heterojunction solar cells, J. Appl. Phys. 109 (12) (2011) 124501, http://dx.doi.org/10.1063/1.3595669. http://link.aip.org/link/JAPIAU/v109/i12/p124501/s1&Agg doi.

[18] T. Monch, P. Guttmann, J. Murawski, C. Elschner, M. Riede, L. Müller-Meskamp, K. Leo, Investigating local (photo-)current and structure of ZnPc:C60 bulk-heterojunctions, Org. Electron. 14 (11) (2013) 2777 2788, http://dx.doi.org/10.1016/j.orgel.2013.07.031. http://linkinghub.elsevier.com/retrieve/pii/S1566119913003467.

[19] D. Nečas, P. Klapetek, Gwyddion: an open-source software for SPM data analysis, Central Eur. J. Phys. 10 (1) (2012) 181 188, http://dx.doi.org/10.2478/s11534-011-0096-2. http://www.springerlink.com/index/10.2478/s11534-011-0096-2.

[20] A. Chowdhury, B. Biswas, B. Mallik, Effects of substrate on the asymmetric grain growth and observation of conductivity anisotropy in nanostructured organic thin films, Sci. Adv. Mater. 5 (9) (2013) 1297 1306, http://dx.doi.org/10.1166/sam.2013.1586. http://openurl.ingenta.com/content/xref?genre article&issn 1947-2935&volume 5&issue 9&spage 1297.

[21] M. Kozlik, S. Paulke, M. Gruenewald, R. Forker, T. Fritz, Determination of the optical constants of α- and β-zinc (II)-phthalocyanine films, Org. Electron. 13 (12) (2012) 3291 3295, http://dx.doi.org/10.1016/j.orgel.2012.09.030. http://linkinghub.elsevier.com/retrieve/pii/S1566119912004569.

[22] S. Pfuetzner, C. Mickel, J. Jankowski, M. Hein, J. Meiss, C. Schuenemann, C. Elschner, A.A. Levin, B. Rellinghaus, K. Leo, M. Riede, The influence of substrate heating on morphology and layer growth in C60:ZnPc bulk heterojunction solar cells, Org. Electron. 12 (3) (2010) 435 441, http://dx.doi.org/10.1016/j.orgel.2010.12.007. http://linkinghub.elsevier.com/retrieve/pii/S1566119910004052.

[23] Z. Bao, A.J. Lovinger, A. Dodabalapur, Organic field-effect transistors with high mobility based on copper phthalocyanine, Appl. Phys. Lett. 69 (20) (1996) 3066, http://dx.doi.org/10.1063/1.116841. http://scitation.aip.org/content/aip/journal/apl/69/20/10.1063/1.116841.

[24] A. Chowdhury, B. Biswas, M. Majumder, M.K. Sanyal, B. Mallik, Studies on phase transformation and molecular orientation in nanostructured zinc phthalocyanine thin films annealed at different temperatures, Thin Solid Films

520 (21) (2012) 6695 6704, http://dx.doi.org/10.1016/j.tsf.2012.07.013. http://linkinghub.elsevier.com/retrieve/pii/S0040609012008620.

[25] H. Claus, Organische Festkorper und organische dünne Schichten, Akademische Verlagsgesellschaft Geest & Porting K.-G, 1978.

[26] D. Roy, N.M. Das, N. Shakti, P.S. Gupta, Comparative study of optical, structural and electrical properties of zinc phthalocyanine langmuir blodgett thin film on annealing, RSC Adv. 4 (80) (2014) 42514 42522, http://dx.doi.org/10.1039/C4RA05417B. http://xlink.rsc.org/?DOI C4RA05417B.

[27] J. Ren, S. Meng, E. Kaxiras, Theoretical investigation of the c60/copper phthalocyanine organic photovoltaic heterojunction, Nano Res. 5 (4) (2012) 248 257, http://dx.doi.org/10.1007/s12274-012-0204-7. http://link.springer.com/10.1007/s12274-012-0204-7.

[28] B.P. Rand, D. Cheyns, K. Vasseur, N.C. Giebink, S. Mothy, Y. Yi, V. Coropceanu, D. Beljonne, J. Cornil, J.-L. Brédas, J. Genoe, The impact of molecular orientation on the photovoltaic properties of a phthalocyanine/fullerene heterojunction, Adv. Funct. Mater. 22 (14) (2012) 2987 2995, http://dx.doi.org/10.1002/adfm.201200512. http://doi.wiley.com/10.1002/adfm.201200512.

[29] Y. Zhang, Y. Diao, H. Lee, T.J. Mirabito, R.W. Johnson, E. Puodziukynaite, J. John, K.R. Carter, T. Emrick, S.C.B. Mannsfeld, A.L. Briseno, Intrinsic and extrinsic parameters for controlling the growth of organic single-crystalline nanopillars in photovoltaics, Nano Lett. 14 (10) (2014) 5547 5554, http://dx.doi.org/10.1021/nl501933q, 140929085647008, http://pubs.acs.org/doi/abs/10.1021/nl501933q.

[30] W. Krakow, N.M. Rivera, R.A. Roy, R.S. Ruoff, J.J. Cuomo, The growth of crystalline vapor deposited carbon-60 thin films, Appl. Phys. A 56 (3) (1993) 185 192. http://link.springer.com/article/10.1007/BF00539472.

[31] P. Peumans, S. Uchida, S.R. Forrest, Efficient bulk heterojunction photovoltaic cells using small-molecular-weight organic thin films, Mater. Sustain. Energy A Collect. Peer Rev. Res. Rev. Artic. Nat. Publ. Group 94 (2003), http://dx.doi.org/10.1038/nature01949. http://www.nature.com/nature/journal/v425/n6954/abs/nature01949.html.

[32] Christoph Schünemann, Organic Small Molecules: Correlation between Molecular Structure, Thin Film Growth, and Solar Cell Performance, TU Dresden, 2012. Ph.D. thesis, http://nbn-resolving.de/urn:nbn:de:bsz:14-qucosa-105169.

[33] C. Elschner, A.A. Levin, L. Wilde, J. Grenzer, C. Schroer, K. Leo, M. Riede, Determining the C60 molecular arrangement in thin films by means of x-ray diffraction, J. Appl. Crystallogr. 44 (5) (2011) 983 990, http://dx.doi.org/10.1107/S002188981103531X. http://scripts.iucr.org/cgi-bin/paper?S002188981103531X.

[34] H.J. Kim, J.W. Kim, H.H. Lee, B. Lee, J.-J. Kim, Initial growth mode, nanostructure, and molecular stacking of a ZnPc:c60 bulk heterojunction, Adv. Funct. Mater. 22 (20) (2012) 4244 4248, http://dx.doi.org/10.1002/adfm.201200778. http://doi.wiley.com/10.1002/adfm.201200778.

[35] C. Schünemann, D. Wynands, L. Wilde, M. Hein, S. Pfützner, C. Elschner, K.-J. Eichhorn, K. Leo, M. Riede, Phase separation analysis of bulk heterojunctions in small-molecule organic solar cells using zinc-phthalocyanine and C60, Phys. Rev. B 85(24). doi:10.1103/PhysRevB.85.245314. URL http://link.aps.org/doi/10.1103/PhysRevB.85.245314

[36] P. Simon, B. Maennig, H. Lichte, Conventional electron microscopy and electron holography of organic solar cells, Adv. Funct. Mater. 14 (7) (2004) 669 676, http://dx.doi.org/10.1002/adfm.200304498. http://doi.wiley.com/10.1002/adfm.200304498.

[37] W. Schindler, M. Wollgarten, K. Fostiropoulos, Revealing nanoscale phase separation in small-molecule photovoltaic blends by plasmonic contrast in the TEM, Org. Electron. 13 (6) (2012) 1100 1104, http://dx.doi.org/10.1016/j.orgel.2012.03.008. http://linkinghub.elsevier.com/retrieve/pii/S1566119912001048.

[38] K. Eichkorn, O. Treutler, H. Ohm, M. Haser, R. Ahlrichs, Auxiliary basis sets to approximate coulomb potentials, Chem. Phys. Lett. 240 (4) (1995) 283 290. http://www.sciencedirect.com/science/article/pii/000926149500621A.

[39] R. Ahlrichs, M. Bar, M. Haser, H. Horn, C. Kolmel, Electronic structure calculations on workstation computers: The program system turbomole, Chem. Phys. Lett. 162 (3) (1989) 165 169, http://dx.doi.org/10.1016/0009-2614(89)85118-8. http://www.sciencedirect.com/science/article/pii/0009261489851188.

[40] A.D. Becke, A new mixing of hartree fock and local density-functional theories, J. Chem. Phys. 98 (2) (1993) 1372, http://dx.doi.org/10.1063/1.464304. http://scitation.aip.org/content/aip/journal/jcp/98/2/10.1063/1.464304.

[41] A. Schafüer, H. Horn, R. Ahlrichs, Fully optimized contracted gaussian basis sets for atoms Li to Kr, J. Chem. Phys. 97 (4) (1992) 2571, http://dx.doi.org/10.1063/1.463096. http://scitation.aip.org/content/aip/journal/jcp/97/4/10.1063/1.463096.

[42] S. Grimme, J. Antony, S. Ehrlich, H. Krieg, A consistent and accurate ab initio parametrization of density functional dispersion correction (DFT-d) for the 94 elements h-pu, J. Chem. Phys. 132 (15) (2010) 154104, http://dx.doi.org/10.1063/1.3382344. http://scitation.aip.org/content/aip/journal/jcp/132/15/10.1063/1.3382344.

[43] C. Hein, E. Mankel, T. Mayer, W. Jaegermann, Engineering the electronic structure of the ZnPc/C60 heterojunction by temperature treatment, Sol. Energy Mater. Sol. Cells 94 (4) (2010) 662 667, http://dx.doi.org/10.1016/j.solmat.2009.10.022. http://linkinghub.elsevier.com/retrieve/pii/S0927024809003778.

[44] J.P. Doye, D.J. Wales, The structure of (c60)n clusters, Chem. Phys. Lett. 262 (1) (1996) 167 174, http://dx.doi.org/10.1016/0009-2614(96)01039-1. http://

www.sciencedirect.com/science/article/pii/0009261496010391.

[45] S. Senthilarasu, Y.B. Hahn, S.-H. Lee, Nano structure formation in vacuum evaporated zinc phthalocyanine (ZnPc) thin films, J. Mater. Sci. Mater. Electron. 19 (5) (2008) 482 486, http://dx.doi.org/10.1007/s10854-007-9368-4. http://link.springer.com/10.1007/s10854-007-9368-4.

[46] J.D. Kotlarski, P.W.M. Blom, L.J.A. Koster, M. Lenes, L.H. Slooff, Combined optical and electrical modeling of polymer:fullerene bulk heterojunction solar cells, J. Appl. Phys. 103 (8) (2008) 084502, http://dx.doi.org/10.1063/

1.2905243. http://scitation.aip.org/content/aip/journal/jap/103/8/10.1063/1.2905243.

[47] L.J.A. Koster, O. Stenzel, S.D. Oosterhout, M.M. Wienk, V. Schmidt, R.A.J. Janssen, Morphology and efficiency: the case of polymer/ZnO solar cells, Adv. Energy Mater. 3 (5) (2013) 615 621, http://dx.doi.org/10.1002/aenm.201200787. http://doi.wiley.com/10.1002/aenm.201200787.

[48] Wolfgang Tress, Device Physics of Organic Solar Cells, TU Dresden, Dresden, 2011. Ph.D. thesis, http://nbn-resolving.de/urn:nbn:de:bsz:14-qucosa-89501.